Fraunhofer IEE

Escuela de Doctorado y Estudios de Posgrado
Universidad de La Laguna

MSc Thesis

Benefits of Grid Forming Inverters in Isolated Electrical Power Systems: The case of Tenerife

Vivek Vinod Balani Mahtani

September 6, 2022

Supervised by:
Benjamín González Díaz[1]
Gunter Arnold[2]

79075490H
alu0100966459@ull.edu.es
vivek.vinod.balani.mahtani@iee.fraunhofer.de
671 472 373

[1]ULL, Department of Industrial Engineering
[2]Fraunhofer IEE, Department of System Stability and Grid Integration

Contents

List of figures ii

List of tables ii

Abstract iv

1 Introduction 1
- 1.1 System inertia . . . 1
- 1.2 Grid Forming vs Grid Following inverters . . . 2
- 1.3 Tenerife's electrical system . . . 3

2 Experimental: materials and methods 9
- 2.1 Equipment . . . 9
- 2.2 Component tests . . . 11
  - 2.2.1 RoCoF events . . . 12
  - 2.2.2 System splits . . . 13
- 2.3 Field tests . . . 14

3 Results and discussion 16
- 3.1 Component tests . . . 16
  - 3.1.1 RoCoF tests . . . 16
  - 3.1.2 System-split tests . . . 18
- 3.2 Field tests . . . 20
  - 3.2.1 RoCoF events with GFL system . . . 20
  - 3.2.2 Microgrids . . . 21
    - 3.2.2.1 Diesel generator . . . 21
    - 3.2.2.2 Wind turbine . . . 23
    - 3.2.2.3 Test houses . . . 24

4 Conclusions 26

Acknowledgements 27

References 28

A RoCoF figures 30

B System split figures 33

List of Figures

1 Differences between GFL and GFM. 2
2 Evolution of the electrical demand in Tenerife. 4
3 Installed power in Tenerife. 4
4 Percentage and amount (MWh) of coverage by each technology in the island of Tenerife. 5
5 Transmission and distribution grid of Tenerife. 6
6 Evolution of the losses in the electrical system of Tenerife. 6
7 Most recent energy faults in Tenerife. 7
8 Equipment for tests. 11
9 Diagram of the RoCoF event tests. 12
10 Diagram of the system split tests. 13
11 Diagram of the field tests. 15
12 Active power response for different RoCoF values 16
13 System split 19
14 Stabilized frequency for different split tests. 19
15 RoCoF events with the grid simulator and test houses. 21
16 Active power and frequency of the GFM, diesel generator and loads. . 22
17 Voltage, current and power quantities of the Diesel generator during the field test. 22
18 Active power and frequency of the GFM, wind turbine and loads. . . 23
19 Voltage, current and power quantities of the Wind turbine during the field test. 24
20 Active power and frequency of the GFM, test houses and loads. . . . 25
21 Voltage, current and power quantities of the test houses during the field test. 25
22 RoCoFs with Ta = 1Ta 30
23 RoCoFs with Ta = 2Ta 31
24 RoCoFs with Ta = 4Ta 32
25 System splits with P = 5kW 33
26 System splits with P = 10kW 34
27 System splits with P = 20kW 35

List of Tables

1 Comparison of Grid-Following and Grid-Forming Controls 3
2 Technological structure of the generation park. 5
3 Overview of the electrical specifications of the GFM prototype. 10
4 Values obtained from ΔP for different sets of values of T_a and RoCoFs. 17
5 Relation by T_a setpoint. 17
6 Relation by RoCoF. 18
7 Obtained T_a for different set values and RoCoFs. 18

Abstract

As the way of generation changes, synchronous generators that provided the necessary services for stable grid operation is being replaced by Inverter Based Resources (IBRs). In this work, the inertia performance of a prototype of a grid forming inverter (GFM) in a microgrid is presented, in order to study the response to frequency events and system split tests. Several field test have been also performed with different energy sources (wind turbine, diesel generator and a PV system with a grid following inverter (GFL).
GFMs are crucial to achieve a 100% renewable based electrical system. Isolated small island are an ideal test ground to start developing these new power sources, and there are several projects in different locations, but none in the Canary Islands. More detailed research and the creation of uniform testing standards are needed to enable quick and secure deployment of GFMs that offer software-based implementation of inertial behaviour.

Keywords: Distributed generation, Grid Forming Inverter, Microgrid, System inertia

Acronyms and abbreviations:

- **AC:** Alternate Current
- **BESS:** Batery Energy Storage System
- **DC:** Direct Current
- **DG:** Distributed Generation
- **GFL:** Grid Following Inverter
- **GFM:** Grid Forming Inverter
- **IBR:** Inverter Based Resource
- **PNI:** *Prüflabor Netzintegration*
- **PV:** Photovoltaic
- **RES:** Renewable Energy Source
- **RoCoF:** Rate of Change of Frequency
- **SSS:** SecondarySubStation
- **TH:** Test House

1 Introduction

Global and fast evolution of electrical power systems carries a wide field of technologies that are based on power electronics to interface with the grid. As the way of generation changes, synchronous generators that provided the necessary services for stable grid operation is being replaced by Inverter Based Resources (IBRs), such as wind, solar and battery energy storage system (BESS). In the upcoming years, with the growing dependence on IBRs, synchronous areas will be operating with 100% IBRs (at least temporarily), which is why this resources must become a primary support for the stability of the system [1].

1.1 System inertia

The inertia of an electrical system is considered to be one of the vital parameters upon which the synchronized operation of any power system is based. In all rotating systems, such as synchronous generators and turbines, it determines the immediate frequency response to inequalities in the overall power balance. After a frequency change occurs, the rotating masses will decelerate or accelerate the rotating systems, and thus feed (or absorb) kinetic energy into (or from) the grid in order to counteract the deviation. This means that the lower the inertia of a complete system, the less damping would be provided and the more nervous the grid frequency reacts to abrupt changes in generation and load patterns [2].

In this matter, isolated grids experience unique challenges. As they are not interconnected with strong mainland grids, the effect of a single event has the potential to have a large impact on the stability of the system. Generation and fuel are more expensive than for larger grids, and because island grids are more vulnerable to the effect of climate change, they may be particularly motivated to transition to a renewable energy-based system. This is why inverters are starting to play a very relevant role in electric power systems [3].

Various sources of information explain inertia testing and how the Grid Forming Inverter (GFM) is evaluated by them. For instance, it is noted in [4] that it is preferable to parameterize the internal behaviour of the GFM in accordance with the synchronous machine's swing equation through the use of the inertia constant H and the damping factor D. The importance and significance of these factors have already been thoroughly studied, therefore it is possible to tailor the GFM's inertial behaviour to existing grids.

A RoCoF test and a system split test method are detailed, together with the findings of a labour experiment, in [5]. With a frequency ramp that is replicated at a grid simulator, for the RoCoF test it is suggested the deactivation of the Damping factor in the internal mechanism of the GFM to determine the Ta parameter. The system split test also offers instructions for calculating the H and D parameters, although their reproducibility is not made clear.

1.2 Grid Forming vs Grid Following inverters

According to [6], inverters provide interfaces to the Distributed Generations (DGs) for grid-interactive operations between energy resources and the power grid, ancillary services for maximum use of the DC bus, mitigate voltage and frequency fluctuations, and provide stability enhancement in grids, among others. As DGs increase, the power grid is expected to be penetrated by a large number of inverter-based generation units.

Inverters can be grid-following (GFL, Figure 1a) or grid-forming (GFM, Figure 1b). The former operate in synchronization with the system and inject a specified amount of active and reactive power, whereas the latter are capable of regulating the voltage and the frequency of the system. This means that grid forming inverters can become a primary source of energy when a microgrid is disconnected from the grid and is needed to operate in an islanded mode.

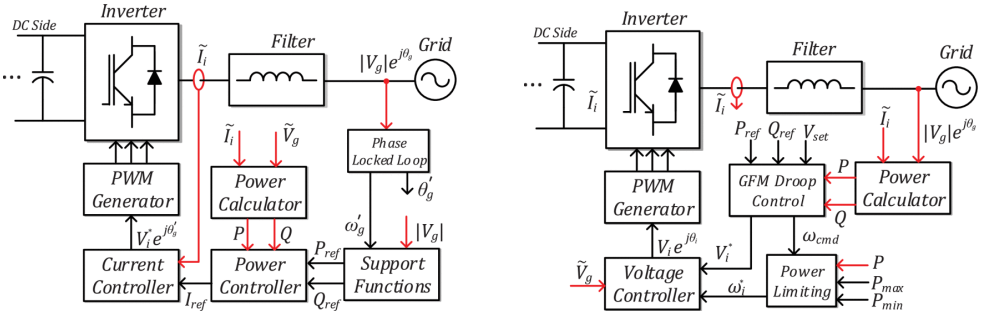

(a) Block diagram of a typical GFL inverter.

(b) Block diagram of a typical GFM inverter.

Figure 1: Differences between GFL and GFM. Extracted from [7].

More specifically, according to [7], GFL inverters control the output of active and reactive power by providing current at a given phase angle. A phase-locked loop is used in order to track the grid phase angle in real time, because the GFL cannot inject regulate frequency or voltage. References are provided from the outside, so if the GFL strays from its voltage or frequency source, it must switch off.

On the other hand, GFM inverters are controllable voltage sources, similar to a grid-bound synchronous generator. These inverters with droop characteristics allow direct control of frequency and voltage. During contingencies, the GFM sources will immediately increase or reduce the output power to balance the loads and maintain the local voltage and frequency values. There shouldn't be a significant delay between the change of output power and the change of output frequency in droop-controlled GFM, which means that there is no relevant time difference between the instantaneous reserve followed by the primary reserve, which starts only few seconds after the frequency change. Thus, GFM sources can respond to any contingencies faster than GFL sources. Providing primary frequency control from

IBRs would mean an enormous advantage, mainly for *low inertia* power systems. Compared to large rotating machines, GFMs are able to change their output faster, arresting system's frequency changes before any load shedding is triggered.

An overview of the main differences between GFI and GFM is given in Table 1.

Table 1: Comparison of Grid-Following and Grid-Forming Controls, extracted from [8].

Inverter Attribute	Grid-Following Control	Grid-Forming Control
Reliance on grid voltage	Relies on well-defined grid voltage, which the control assumes to be tightly regulated by other generators (including GFM inverters and synchronous machines)	Actively maintains internal voltage magnitude and phase angle
Dynamic behavior	Controls current injected into the grid (appears to the grid as a constant current source in the transient time frame)	Sets voltage magnitude and frequency/phase (appears to the grid as a constant voltage source in the transient time frame)
Reliance on PLL for synchronization	Needs PLL or equivalent fast control for synchronization	Does not need PLL for tight synchronization of current controls, but may use a PLL or other mechanism to synchronize overall plant response with the grid.
Ability to provide black start	Not usually possible	Can self-start in the absence of network voltage. When designed with sufficient energy buffer and over-current capability, it can also restart the power system under blackout conditions. (Only a limited number of generators on a system need to be black start-capable.)
Ability to operate in low grid strength conditions	Stable operation range can be enhanced with advanced controls, but is still limited to a minimum level of system strength	Stable operation range can be achieved without a minimum island. (GFM IBRs will not, however, help to resolve steady-state voltage stability for long-distance high-power transfer.)
Field deployment and standards	Has been widely used commercially. Existing standards and standards under development define its behavior and required functionalities well	Has been deployed in combination with battery storage primarily for isolated applications. Very limited experience exists in interconnected power systems. Existing standards do not yet define its behavior and required functionalities well.

1.3 Tenerife's electrical system

The island of Tenerife is an isolated electricity system of small size compared to continental systems. Energy consumption per inhabitant is well below that of European regions, due to the mild and stable climate throughout the year and the low intensity of the industrial sector. Currently, 97% of primary energy comes from fossil fuels, and although the electricity sector is the most likely to integrate renewables, these only represent around 21% in the case of Tenerife, according to [9].

In Fig. 2 the evolution of the electrical demand of the system is shown. Since the late 90s it has increased up to around 3,5 GWh, where it stabilized, until the past year 2020, due to COVID-19.

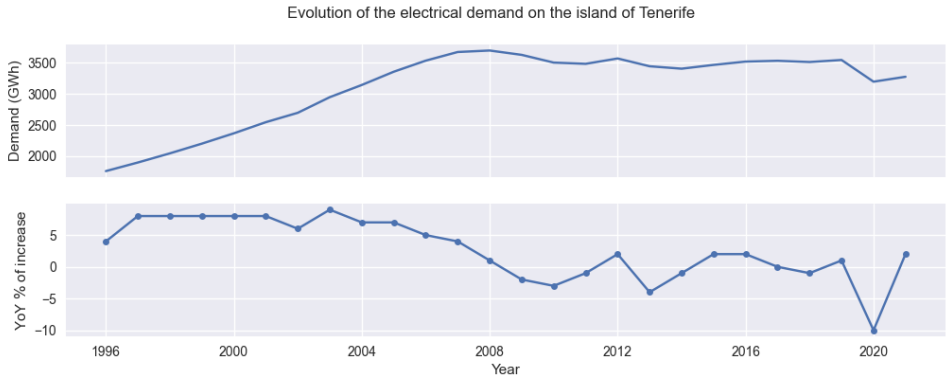

Figure 2: Evolution of the electrical demand in Tenerife. Self developed with data from [9] and [10].

Figs. 3 and 4 show the penetration of IBRs in the island's electrical system and the evolution of the installed power. The difference between 2018 and 2019 is due to the fact that on the 5^{th} October 2018, three years after the introduction of the controversial *solar tax*, Teresa Ribera, Spanish Ministress for Ecological Transition, announced its end. She also added a series of reforms to encourage the use of solar energy in Spain. The following year, the current regulation RD 244/2019 was approved, with the aim of simplifying administrative procedures.

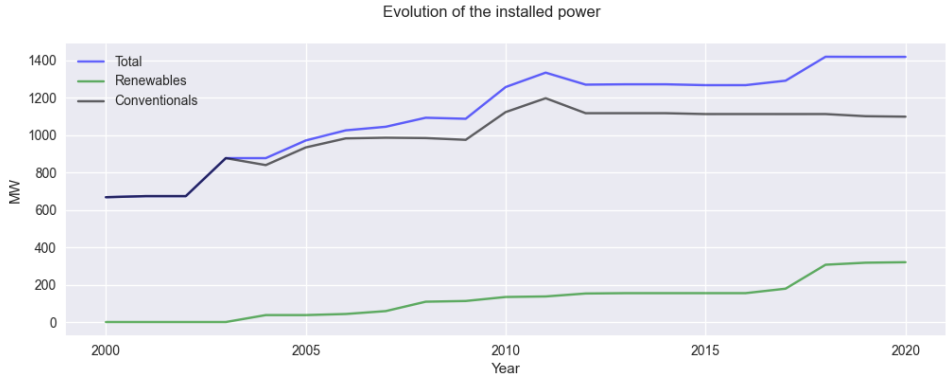

Figure 3: Installed power in Tenerife. Self developed with data from [9].

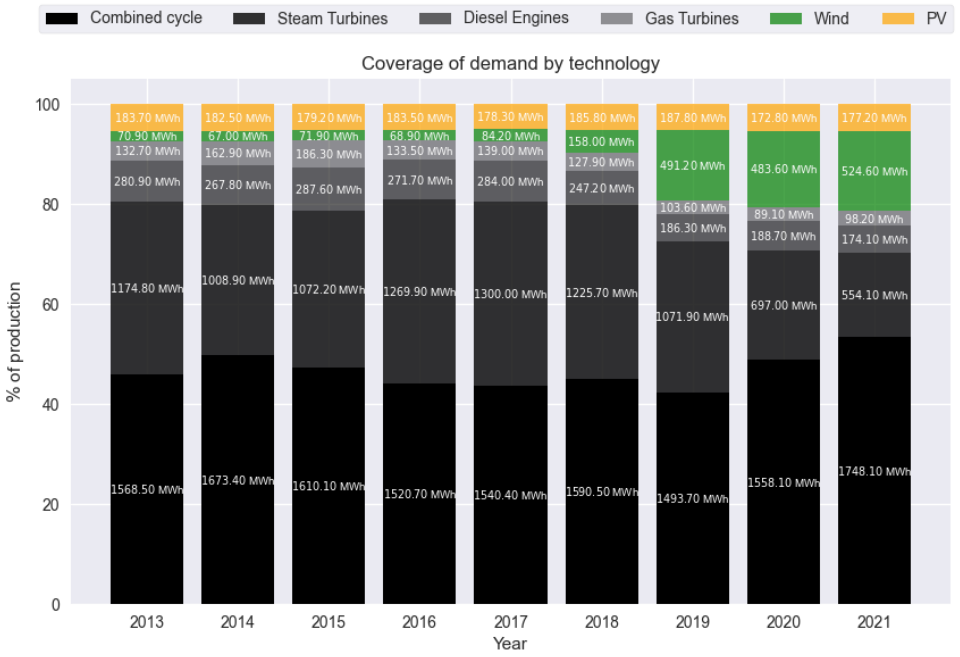

Figure 4: Percentage and amount (MWh) of coverage by each technology in the island of Tenerife. Self developed with data from [9] and [10].

Table 2: Technological structure of the generation park. Data extracted from [9].

	Technology	Installed Power [MW]
Thermal	Steam turbine	240,00
	Diesel engine	84,00
	Gas turbine	265,70
	Combined cycle	456,80
Refinery	Steam turbine	25,90
Cogeneration	Diesel engine	2,20
	Gas turbine	37,00
Total conventional		1111,60
Renewables	Wind	195,65
	Photovoltaics	107,21
	Mini-hydro	1,22
	Biogas	1,60
Total renewables		305,68
Total		1417,28

Currently, the generation park is structured as shown in Table 2.

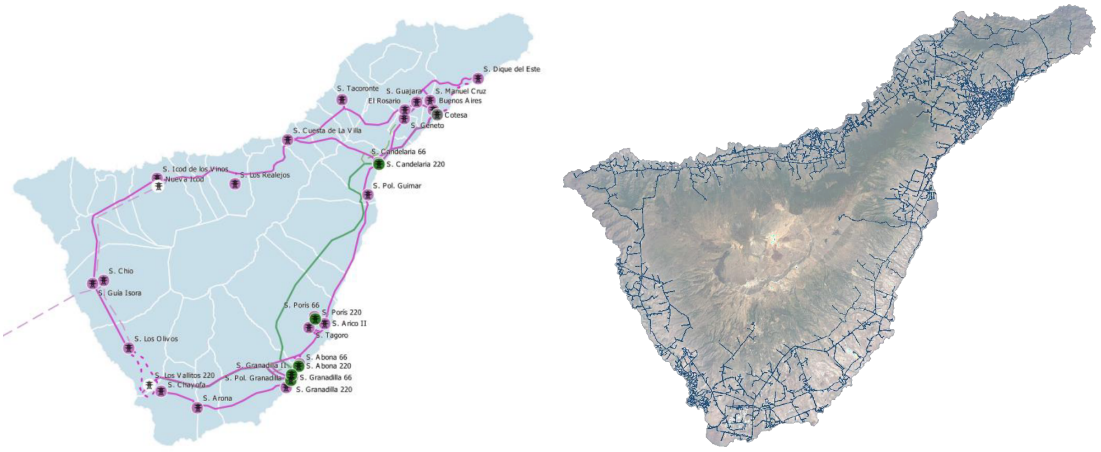

(a) Transmission grid. (b) Distribution grid.

Figure 5: Transmission and distribution grid of Tenerife. Extracted from [9].

Regarding the transmission grid in Tenerife (Fig. 5), it is made up of 21 66kV substations, 6 220kV substations (5 currently operational) and 45 lines, totaling 584 km, comprising 494.2 km of overhead cable and 90.72 km underground (data provided by REE).

Losses in the distribution and transmission grid have decreased over the years, as shown in Fig. 6. Nevertheless, in 2020, the average was 7.82% of the energy fed into the grid, an increase of 8.1% compared to the previous year.

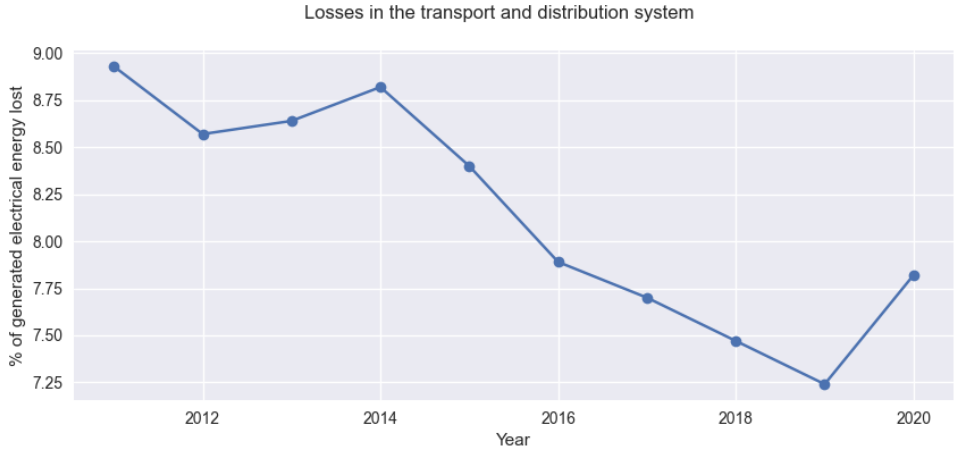

Figure 6: Evolution of the losses in the electrical system of Tenerife. Self developed with data from [9] and [10].

The electrical system of Tenerife is also very weak. As an isolated grid, a single fault can mean a complete blackout of the entire island. Recently, as shown in Fig. 7,

there were two very near in time blackouts, one on 29^{th} September 2019 and the following on 15^{th} July 2020.

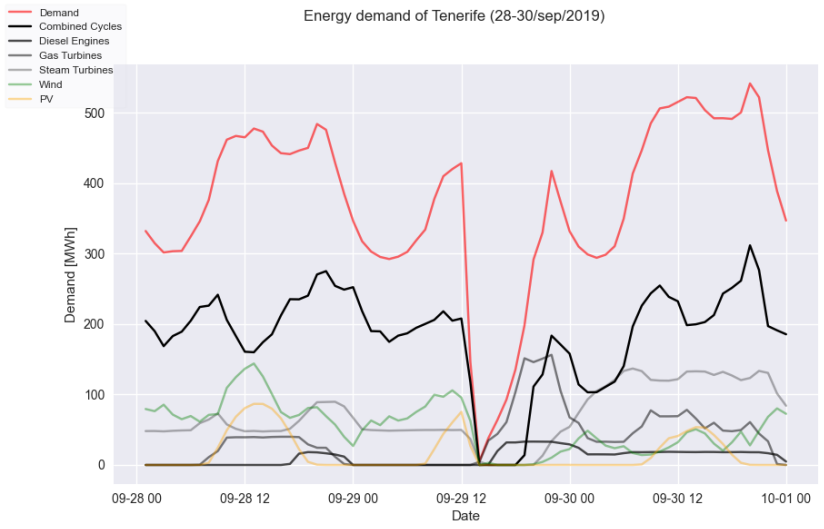

(a) Fault on 29/09/2019.

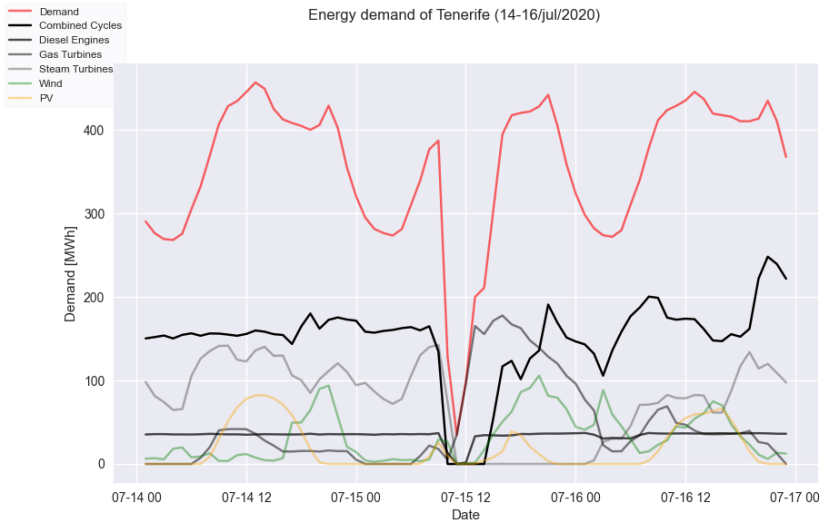

(b) Fault on 15/07/2020.

Figure 7: Most recent faults in Tenerife. Self developed with data from [10].

Between 2009 and 2010 there were three other major blackouts. On 26^{th} March 2009, a lightning strike on a 66 kV transmission line between Güímar and Arico left Tenerife without electricity. Almost a year later, on 18^{th} February 2010, a short circuit caused by water leaking from the roof of the Las Caletillas power station repeated the scene. The third one happened less than a month later, in the early hours of 1^{st} March of the same year. At 1.19 am, a fault in the 66 kV side of

Candelaria's substation caused the entire output of Las Caletillas power station to be disconnected and, as an immediate consequence, Granadilla's power station disconnected as well. This affected the entire electricity supply on the island. On the latter occasion, power was restored in six and a half hours. However, in terms of blackouts, the most serious occurred in 2005 during the tropical storm Delta, which affected the Canary Islands, and especially Tenerife. The destruction of the power lines left more than $300,000$ people without power. The thorniest part, however, was that in some areas of Santa Cruz, La Laguna, Tegueste, Arico, Fasnia and Güímar the electricity supply was not restored until seven days later.

According to [11], islanded subsystems within the distribution system can be the result either of a planned split of a subsystem at a set point of the grid under certain contingencies, unintentional islanding in case of a system separation from the transmission system, or the result of local restoration after a complete blackout. This last one can start from both, plants that underwent a successful transition to *house-load* islanding mode or with the black start of generation units.

Also, if no neighbouring grid strong enough to provide voltage and power is available, system restoration can either begin with power plants able to switch to *house-load* island operation or with black-start units. Both features are not often implemented within Renewable Energy sources (RES) today due to regulation, although it is technically possible. RES do not need much auxiliary power and only a short period of time for being able to start operating. If a DG grid was developed based on GFMs, several damages would have been avoided during these events on the island of Tenerife (if the REs were available during the events).

Islands are often the first to achieve extremely high instantaneous IBR levels. Because of this, island power systems, like Tenerife, are used as proving grounds to develop and present technologies that will probably be implemented in mainland power grids during the next few years.

Thus, the aim of this work is to determine the benefits and to assess the performance of a prototype of a GFM in a microgrid, in order to study the response to RoCoF events and system split tests, with and without other power sources.

2 Experimental: materials and methods

2.1 Equipment

To achieve the objective of this work, the following equipment was used:

- **GFM Prototype (EUT):** Designed and developed by the Power Electronics department of the Fraunhofer IEE, Fig. 8a. An overview of the electrical specifications of the GFM prototype is shown in Table 3.
- **Regatron DC Source:** It is a high-power DC source-sink unit with bidirectional output. With an active Power Factor Correction, the wideband AC input module can accept many AC grid systems from around the world. "Quadrant crossover" between source and sink operation and vice versa is made possible by the bidirectional converter architecture, and under ohmic load, a full current source to full current sink action only requires roughly 3 ms. [12], Fig. 8b.
- **AC Grid simulators:** used to simulate the RoCoF events. Two of them were used:
  - AMETEK RS Series: It consists of numerous highly efficient AC and DC power units that deliver controlled AC and DC output for Automatic Test Equipment (ATE) and product test applications [13], Fig. 8c.
  - Gustav Klein: It is a LV-AC-network simulator, with a rated capacity of 1000 kVA. It allows a frequency range of 45-65 Hz.
- **Wind turbine NPS 100:** with a rated capacity of 95 kW, connected with a GFL inverter Fig. 8d.
- **Diesel Generator:** with a rated power of 200 kVA, Fig. 8e.
- **Test houses:** two houses with *on-roof-mounted* PV systems (7 and 5 kW), each with a GFL inverter Fig. 8f. The inverters are one Sunny Tripower 5000TL-20 and one Sunny Tripower 9000TL-20, with a rated capacity of 5 kW and 9 kW respectively.
- **RLC load banks:** a set of loads to simulate the energy demand of the system, Fig. 8e.

Table 3: Overview of the electrical specifications of the GFM prototype.

Apparent power	S = 45 kVA
Nominal line-to-line Voltage	$V_{AC} = 400V$
Maximum line-to-line Voltage	$V_{AC,max} = 620V$
Switching Frequency SiC	$f_{sw,SiC} = 72kHz$
Power Factor at Nominal Current	$PF = 0.03...1.00$
Power Density	$0.81kW/kg$ $0.84kW/l$

Regarding the measurement devices, the following were used:

- **Dewetron DEWE-2600:** Up to 80 analog channels are available in this compact all-in-one measurement tool. The sampling rate is up to 10MS/s per channel with 16, 22, or 24-bit resolution, and each channel has its own anti-aliasing filter [14]. It was used to measure the output of the GFM prototype and the loads inside the PNI.
- **KoCos EPPE W8:** It is a highly accurate power quality analyzer that thoroughly records voltage, current, and power quantities to allow the validity of network parameters to ensure compliance with acceptable quality requirements [15]. Three similar devices were used to measure the output from the wind turbine, the diesel generator and the loads in the SSS2. In Fig. 8e, 2 of them are shown.

The postprocessing and visualisation of the data was developed with *Python*. The output files from the Dewe-2600 were read directly with the *dwdatareader* library, and transformed into a *Pandas* dataframe, to easily work with them. Regarding the EPPE W8 data, it first had to be exported to *csv* files in order to work with them in *Pandas*. Data visualization was done with *Matplotlib*, which is one of the most used *Python* libraries to develop plots and figures.

(a) GFM prototype.

(b) DEWE-2600 and DC source.

(c) AC grid simulator.

(d) Wind turbine.

(e) LV cabinet of the Diesel genset and loads (with EPPE W8 devices).

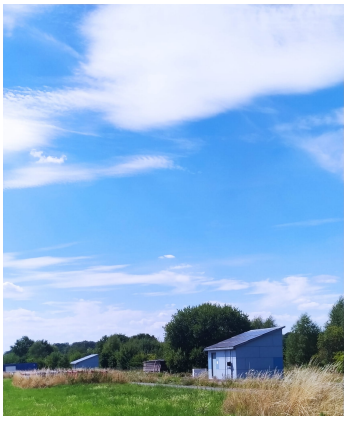

(f) Test houses.

Figure 8: Equipment for tests.

With these devices, different tests were performed: component tests (such as RoCoF events and system split tests), and field test, in order to assess the behaviour of the prototype in a microgrid.

2.2 Component tests

The goal with these tests is to determine the parameters of the transfer function of the GFM prototype, which is:

$$G(s) = \frac{1}{s \cdot T_a + D} \tag{1}$$

where T_a is the acceleration time constant and D is the damping coefficient.

2.2.1 RoCoF events

The applied RoCoF testing procedure is based on the methodology reported in prEN 50549-10 [16]. The goal is to calculate the active power drift (ΔP) that results from frequency events using a fixed RoCoF specification in order to derive the acceleration time constant (T_a) from Eq. (2),

$$T_a = \frac{f_n}{RoCoF} \cdot \frac{\Delta P}{S_n} \tag{2}$$

where S_n is the rated power of the GFM prototype (43.5 kVA) and f_n is the nominal frequency of the system (50 Hz). This acceleration time constant is related to the inertia constant (H) of the GFM as follows:

$$T_a = 2 \cdot H \tag{3}$$

In Fig. 9 a diagram of the system is shown. As a set parameter of the time constant T_a, the values of 5, 10 and 20 s were chosen (T, 2T and 4T). The GFM was considered as a *black-box*, so different fixed RoCoF values (0.10, 0.20, 0.33, and 0.50 Hz/s) were used. This was carried out with the two different AC grid simulators, in order to assess the reproducibility of the tests.

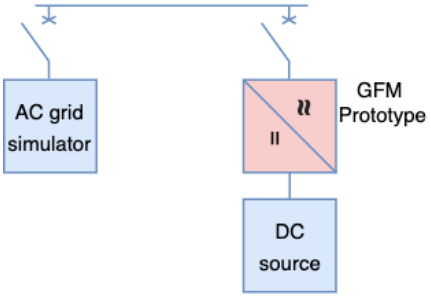

Figure 9: Diagram of the RoCoF event tests.

A RoCoF event is applied for a set period of time until it reaches the new frequency operating point f_{over} (or f_{under}), starting with an operating point at a predefined frequency value of 50 Hz. The frequency is then adjusted with another RoCoF event until it reaches f_{under} (or f_{over}). Finally, with the same RoCoF, the frequency is again set to the nominal value of the grid, 50 Hz.

2.2.2 System splits

On the other hand, to determine the inertia behavior of the GFM, system split tests were carried out. When the microsystem formed by the different loads and the prototype was disconnected, the characteristic P(f) of the GFM was studied. An overview of the system is shown in Fig. 10.

The procedure of these tests consists of 3 phases: first of all, the GFM and the loads are connected to the public network. Subsequently, the disconnection is performed abruptly, by opening the switch after T1. Finally, the GFM stabilizes at a steady-state frequency by increasing or decreasing its output power, depending on the load that needs to be covered.

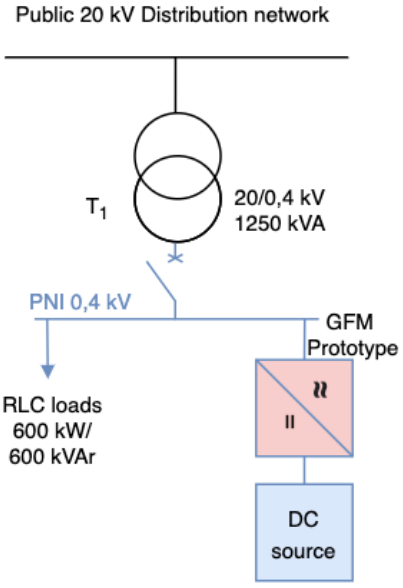

Figure 10: Diagram of the system split tests.

With these tests, the Damping coefficient can be calculated from the following relation:

$$D = \frac{\Delta P_{pu}}{\Delta f_{pu}} \tag{4}$$

where ΔP_{pu} is the variation of the active power per unit between the output of the GFM before the split and the steady-state after the split, and Δf_{pu} is the variation of the frequency in the same period.

The damping factor D influences the rotor swings in the occurrence of a frequency event, which affects the stability of the rotor angle. It is essential that the GFM offers damping that is comparable to the damping torque of synchronous machines (SMs).

Then, according to [5], multiplying this damping coefficient D by the device's time constant yields the acceleration time constant T_A Eq. (5).

$$T_A = \tau \cdot D \tag{5}$$

By calculating the time at which 63% of the steady-state frequency deviation Δf_{stat} is reached, it is possible to estimate the value of τ:

$$\Delta f(t = \tau) = 1 - e^{-t/\tau} = 1 - e^{-1} \approx 0.63 \tag{6}$$

Simulated test cases include situations where the GFM's active power setpoint is equal to the parallel load, below the load (the surplus load case), and above the load (surplus generation case).

2.3 Field tests

As the main goal of this work is to determine the behaviour of the GFM prototype in a microgrid, several field tests were carried out. To do so, the different power supply systems mentioned in the equipment were turned on. On one of the test days, the wind turbine was able to operate. On another test day, a combination of the test houses and the diesel generator was used to form the microgrid.

A similar procedure to the one described above was developed. First, the system was connected to the public network, and then an abrupt disconnection was carried out, by opening the switch from the 20 kV distribution network busbar. A simplified diagram of the system is shown in Fig. 11.

Regarding the microgrid formed by the GFM and the test houses, also several RoCoF events were performed, in order to evaluate the active power response of the GFM coupled with a GFL system.

Unfortunately, no black-starts were carried out, since the GFM prototype was not completely developed.

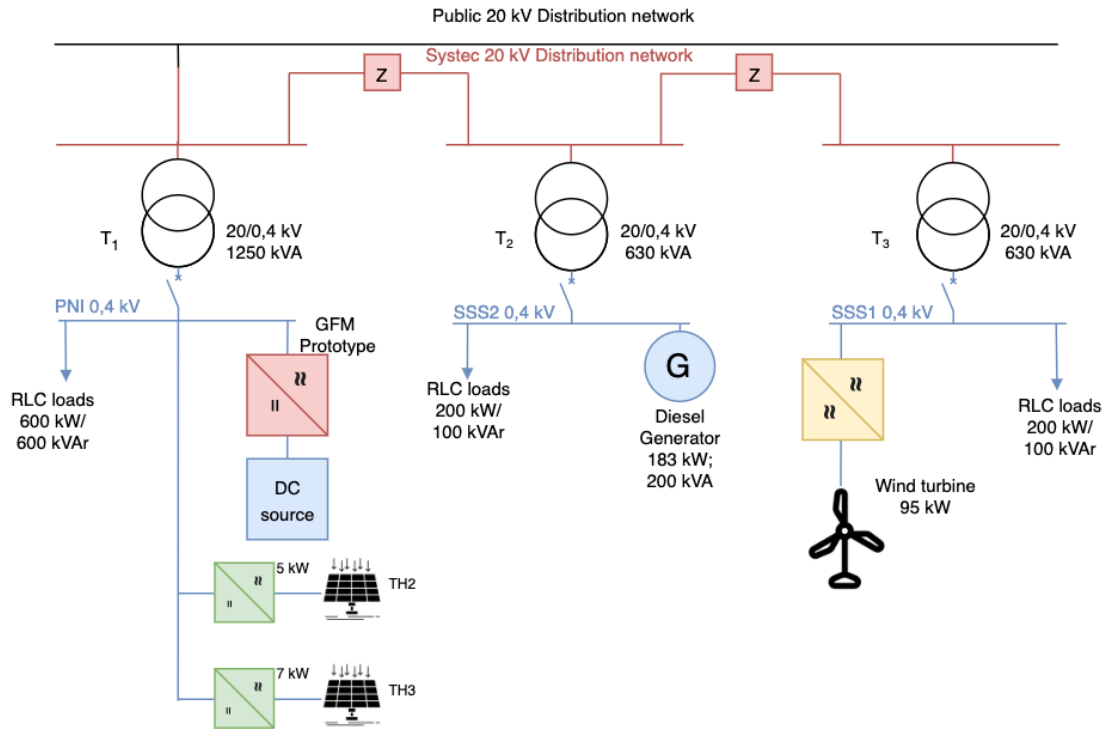

Figure 11: Diagram of the field tests.

3 Results and discussion

In this section the obtained results of the different tests in are presented.

3.1 Component tests

3.1.1 RoCoF tests

Regarding the RoCoF event tests, the main results are presented in Table 4. The relation between the values obtained of ΔP is always very close to double when increased by 2 the set point of the acceleration time constant of the prototype, which means that the GFM behaves as expected according to Eq. (2).

Some of the tests are displayed in Fig. 12. Due to the longer time required for the GFM to reach the steady-state value of the active power, the step from 49 Hz to 51 Hz (or vice versa) was used to calculate ΔP. In Appendix A all the tests are presented.

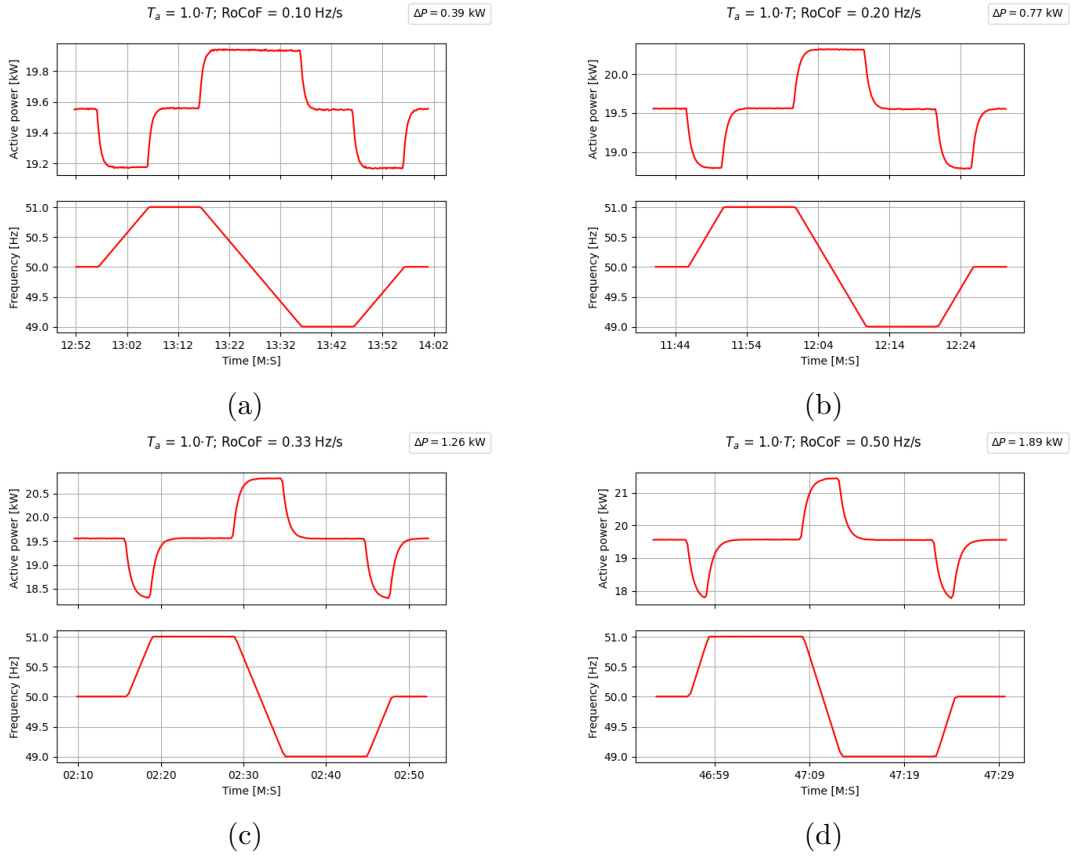

Figure 12: Active power response for different RoCoF values

Table 4: Values obtained from ΔP for different sets of values of T_a and RoCoFs.

Rocof [Hz/s]	$\Delta P[kW]$; $T_a = T$	$\Delta P[kW]$; $T_a = 2T$	$\Delta P[kW]$; $T_a = 4T$
0.10	−0.39	−0.76	−1.51
0.20	−0.77	−1.50	−2.99
0.33	−1.26	−2.49	−4.96
0.50	−1.89	−3.72	−7.41
−0.10	0.39	0.76	1.51
−0.20	0.77	1.51	3.00
−0.33	1.26	2.50	4.97
−0.50	1.89	3.73	7.43

Table 5 shows the relation between the obtained values of ΔP for consecutive set points of T_a. This value should be close to 2, as mentioned above. The gratest deviation is of 2.60%, which means that none of the values is below 1.948.

Table 5: Relation by T_a setpoint.

Rocof [Hz/s]	$\frac{\Delta P(2T)}{\Delta P(T)}$	Deviation	$\frac{\Delta P(4T)}{\Delta P(2T)}$	Deviation
0.10	1.949	2.56%	1.987	0.66%
0.20	1.948	2.60%	1.993	0.33%
0.33	1.976	1.19%	1.992	0.40%
0.50	1.968	1.59%	1.992	0.40%
−0.10	1.949	2.56%	1.987	0.66%
−0.20	1.961	1.95%	1.987	0.66%
−0.33	1.984	0.79%	1.988	0.60%
−0.50	1.974	1.32%	1.992	0.40%

The active power drift should also have a linear relationship with the different RoCoF value, as shown in Table 6. The greatest deviation is of 1.32%, between the values of 0.20 and 0.10 Hz/s and for the set time constant of 10 s.

Table 6: Relation by RoCoF.

	$T_a = T$		$T_a = 2T$		$T_a = 4T$	
$\frac{RoCoF_2}{RoCoF_1}$	$\frac{\Delta P(RoCoF_2)}{\Delta P(RoCoF_1)}$	Deviation	$\frac{\Delta P(RoCoF_2)}{\Delta P(RoCoF_1)}$	Deviation	$\frac{\Delta P(RoCoF_2)}{\Delta P(RoCoF_1)}$	Deviation
$\frac{0.20}{0.10} = 2.00$	1.97	−1.28%	1.97	−1.32%	1.98	−0.99%
$\frac{0.33}{0.20} = 1.65$	1.64	−0.83%	1.66	0.61%	1.66	0.54%
$\frac{0.50}{0.33} = 1.52$	1.50	−1.00%	1.49	−1.40%	1.49	−1.40%
$\frac{-0.20}{-0.10} = 2.00$	1.97	−1.28%	1.99	−0.66%	1.99	−0.66%
$\frac{-0.33}{-0.20} = 1.65$	1.64	−0.83%	1.66	0.34%	1.66	0.40%
$\frac{-0.50}{-0.33} = 1.52$	1.50	−1.00%	1.49	−1.53%	1.49	−1.33%

Once the values of ΔP have been obtained, it is possible to calculate the actual value of the time constant T_a, using Eq. (2). In Table 7 a summary of the results is shown.

Table 7: Obtained T_a for different set values and RoCoFs.

Rocof [Hz/s]	Calculated T_a for set 5 s	Deviation	Calculated T_a for set 10 s	Deviation	Calculated T_a for set 20 s	Deviation
0.10	4.33	−13%	8.44	−16%	16.78	−16%
0.20	4.28	−14%	8.33	−17%	16.61	−17%
0.33	4.24	−15%	8.38	−16%	16.70	−16%
0.50	4.20	−16%	8.27	−17%	16.47	−18%
−0.10	4.33	−13%	8.44	−16%	16.78	−16%
−0.20	4.28	−14%	8.39	−16%	16.67	−17%
−0.33	4.24	−15%	8.42	−16%	16.73	−16%
−0.50	4.20	−16%	8.29	−17%	16.51	−17%

The results show a similar accuracy between a 13 and a 18% deviation. This large deviation is not only caused by measurement uncertainty, but mainly due to the complex GFM control structure. Nevertheless, it is a very important fact that the values obtained increase similarly to the increase of the set point, which means that when moving to the right in the table, the values are multiplied by 2, as should be.

3.1.2 System-split tests

Several tests were conducted for partial grid functioning using various active power setpoints for the GFM prototype and loads. In Fig. 13 an example of the 3 phases mentioned before can be seen (public network, abrupt disconnection and stabilization). The rest of the test are grouped in Appendix B.

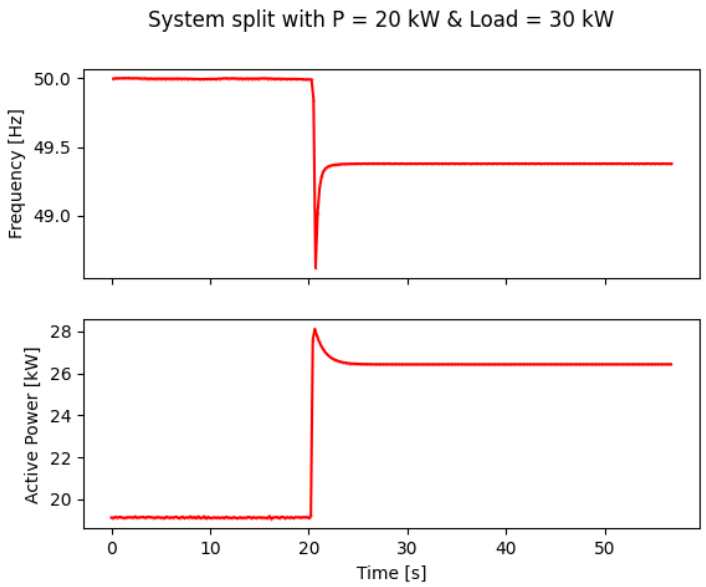

Figure 13: System split

A plot of the stabilised frequency following the induction of the system split may be seen in Fig. 14. It is significant to observe that the slopes of the three active power setpoints are remarkably comparable, indicating that the GFM functions similarly regardless of the power feeding into prior to the split.

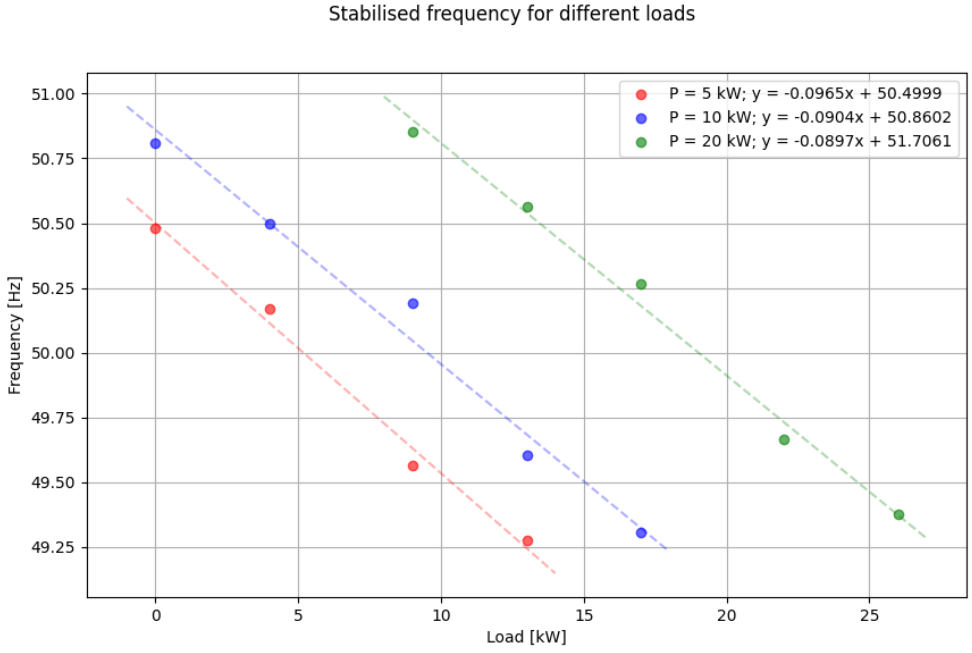

Figure 14: Stabilized frequency for different split tests.

Regarding the damping coefficient, as can be seen in Fig. 13, the transient during the abrupt disconnection of the system is too short to study the value of the acceleration time constant with Eqs. (5) and (6). Also, the loads used in the laboratory were also voltage and frequency dependent, so the mentioned method of determining the Damping and, thus, the acceleration time constant, cannot be calculated in this case.

3.2 Field tests

3.2.1 RoCoF events with GFL system

To verify the behavior of the GFM prototype coupled with a GFL system, several RoCoF events were carried out. The results are shown in Fig. 15. It can be seen that as frequency rose, both IB systems lowered their active power output, in order to counteract the overfrequency. Once the frequency was restored to below the 50.2 Hz limit, the active power output increased to the set point in the case of the GFM and to the available power given by the irradiance at the moment in the GFL case.

Nevertheless, regarding the underfrequency event (beginning at 11:53:06), only the GFM was able to increase its power output to counteract the event. This seems obvious, because the GFL is unable to increase its output if the actual production of the PV system does not increase. Actually, it is currently not required in Germany for GFL PV inverter to increase power output in case of underfrequency events, allthough it is required for BESS inverter (also with GFL). The requirement mainly depends from the primary energy technology (battery, combustion engine, Wind, PV), not from the converter.

When combining a GFM inverter with a true DC system, such as PV, this information is crucial. If the GFM's output active power is at its maximum when the frequency decreases, it will not be able to boost it to offset the underfrequency event.

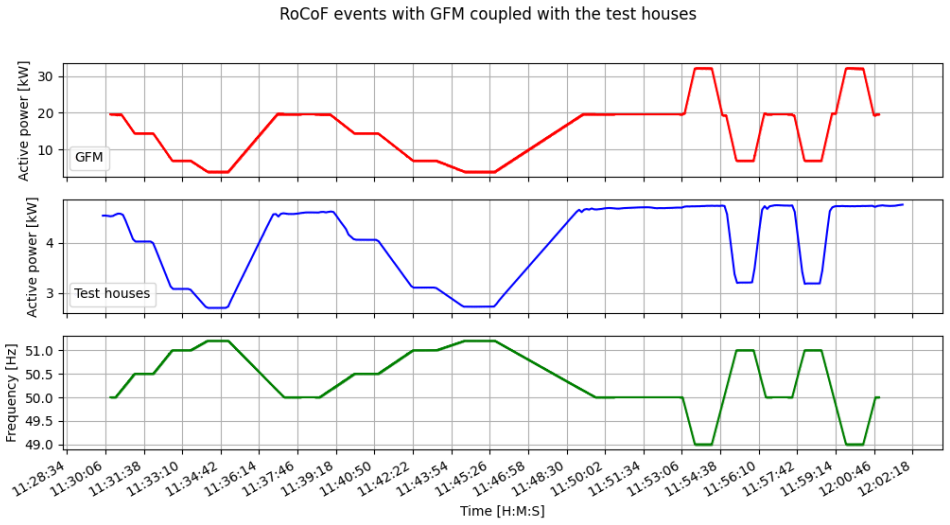

Figure 15: RoCoF events with the grid simulator and test houses.

3.2.2 Microgrids

3.2.2.1 Diesel generator

In Fig. 16 a plot of one successful microgrid is shown between the diesel generator and the GFM prototype. The system was able to cover the loads for about 5 minutes, but afterwards, the diesel generator disconnected as shown in Fig. 17. Since the connection was as shown in Fig. 11, the Diesel generator was mainly supplying the loads in SSS2 and the GFM prototype the loads in PNI.

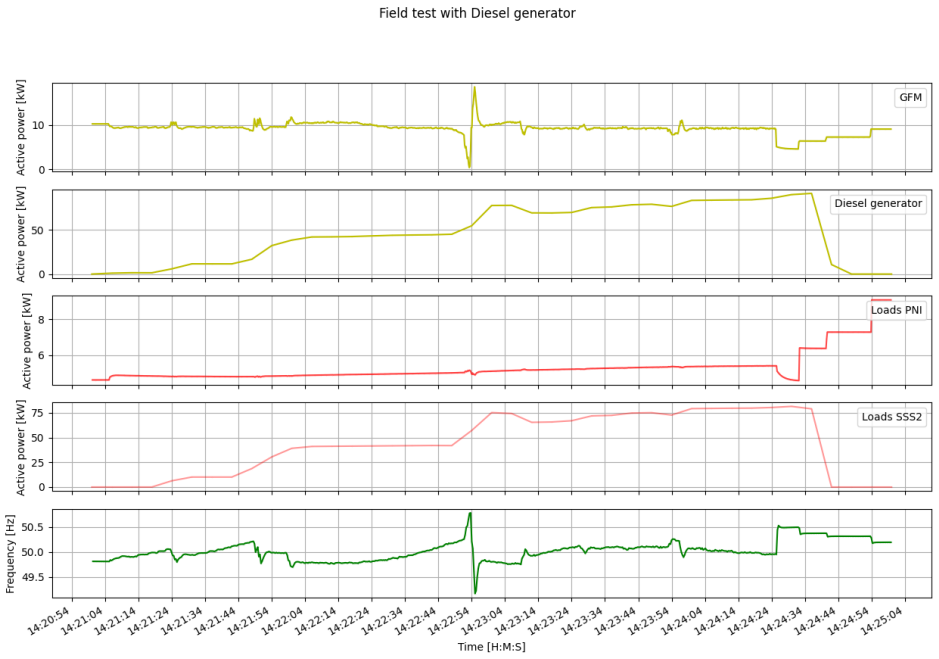

Figure 16: Active power and frequency of the GFM, diesel generator and loads.

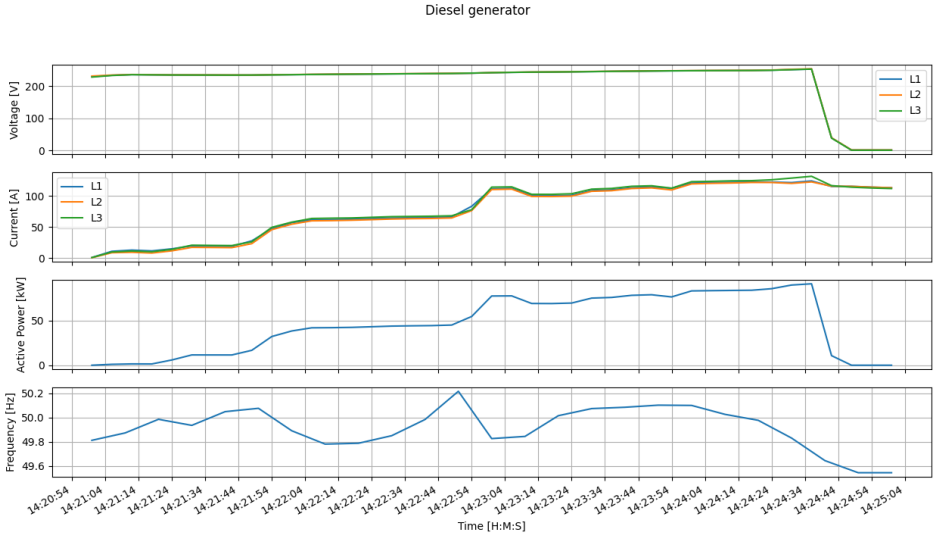

Figure 17: Voltage, current and power quantities of the Diesel generator during the field test.

It is important to mention that the frequency measured by the EPPE W8 (data in

Fig. 17) was measured only every 6 s, and the frequency gathered by the DEWE-2600 (Fig. 16) was measured with a frequency of 20kHz. This is why the frequency plots look different in Figs. 16 and 17.

3.2.2.2 Wind turbine

Regarding the coupling with the wind turbine, the resource during the test days was not very abundant, so the maximum active power supplied by the wind turbine was only 20 kW (which is 0.21pu). In Fig. 18 a plot of the values collected from the measurement devices is shown during a 7-minute microgrid. It is noticeable that the frequency is not as stable as with the Diesel generator, because the only frequency source is the GFM prototype, since the wind turbine is connected to a GFL.

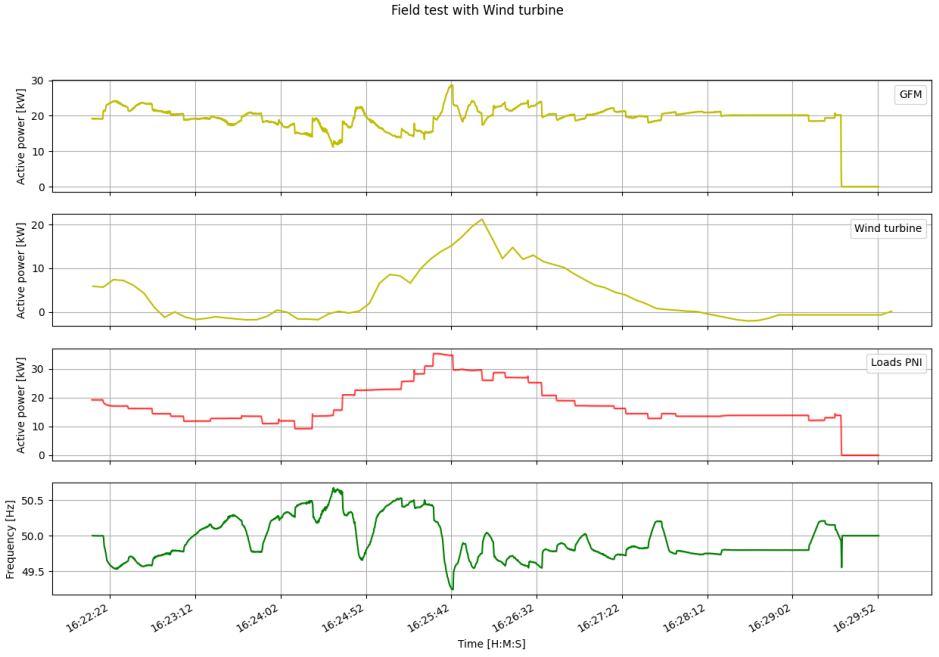

Figure 18: Active power and frequency of the GFM, wind turbine and loads.

In Fig. 19 the electrical parameters of the wind turbine during the test are shown.

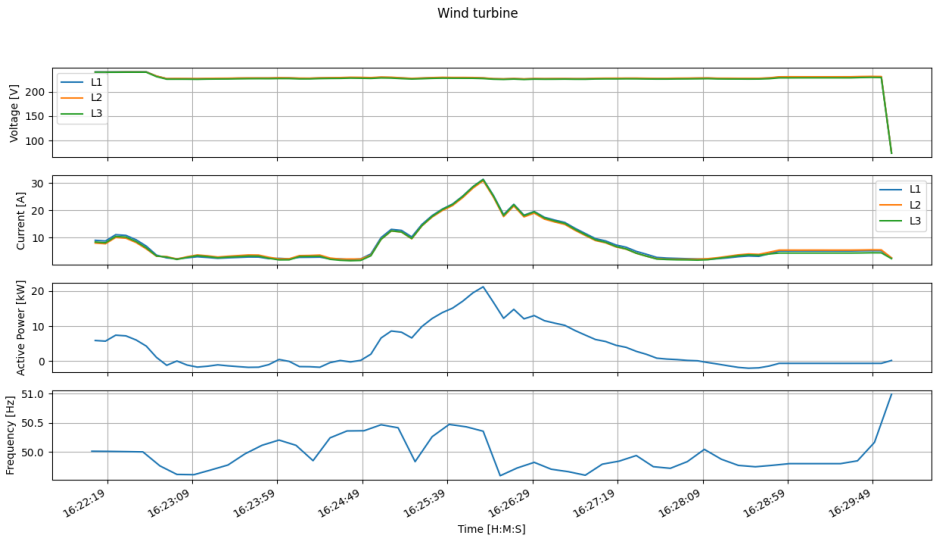

Figure 19: Voltage, current and power quantities of the Wind turbine during the field test.

As in the previous case, the frequency measured by the EPPE W8 was every 6 s, while the frequency measured by the DEWE-2600 was measured every 50 μs, which explains the difference between Figs. 18 and 19 in the frequency plot.

3.2.2.3 Test houses

The most relevant case for the topic of this work is the coupling of the GFM with a PV connected GFL. A successful field test utilising the distribution depicted in Fig. 11 (with only the prototype, the test houses, and the loads in the PNI) is shown in Fig. 20. The system was able to supply the loads for approximately 15 minutes, even when they changed. After a load increase, the GFM prototype was adjusting its power output regarding the supply of the GFL system. Once the test houses reached the peak value (irradiance reached a constant value with no clouds), the GFL also reduced its active power output as requested by the German LV grid code, and the GFM prototype regulated the frequency of the system.

In Fig. 21 a plot of the electrical parameters of the test houses during the field test is shown.

Similarly to the 2 above cases, the frequency plot difference in Figs. 20 and 21 is due to the measurement capacity of the 2 used devices.

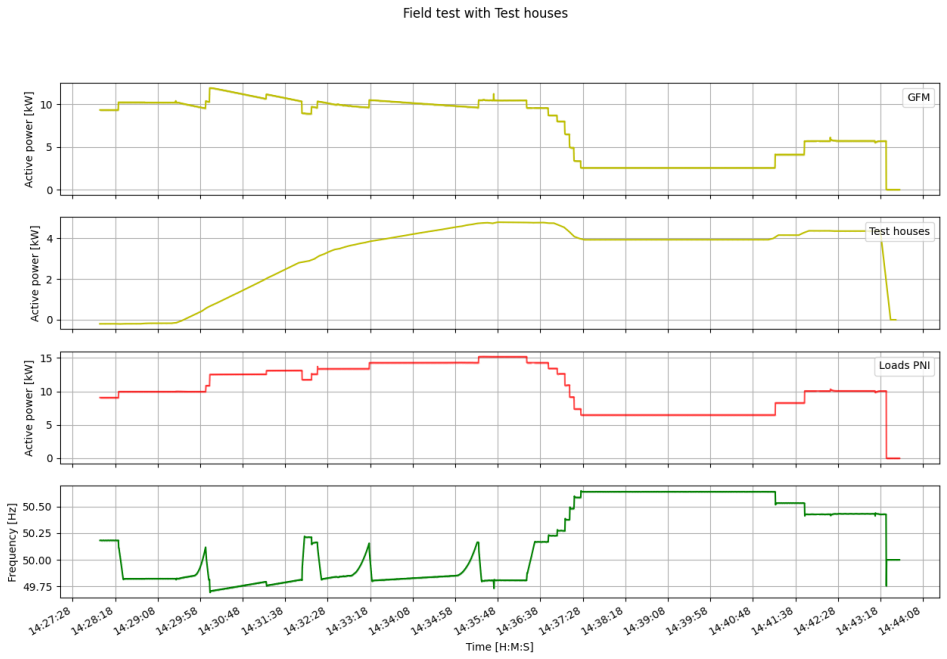

Figure 20: Active power and frequency of the GFM, test houses and loads.

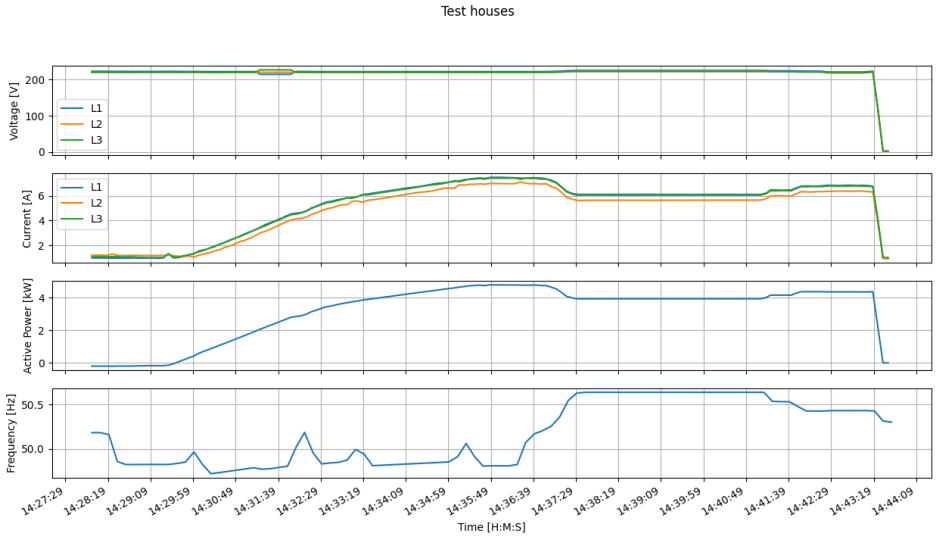

Figure 21: Voltage, current and power quantities of the test houses during the field test.

4 Conclusions

In this work several laboratory and field tests were carried out to determine the behaviour of a GFM prototype in an electrical system. The prototype is capable of providing synthetic inertia (also found as electric or virtual inertia) and responds correctly to over and under frequency events. It was also successful when separated from the public network and loads were demanding active power, with and without other power sources in the system. The coupling with one GFL inverter based system was also necessary, because currently most of the PV systems that have been deployed in Tenerife (self-consumption and grid-connected) are grid-following.

Unfortunately, no black-starts were carried out with the prototype since it was not fully developed, it is not possible to reach to conclusions about the capability of restarting the system after a black out.

Although the tests were carried out with low power, it can be concluded that grid forming inverters are crucial to achieve a 100% renewable based electrical system. Isolated small island are an ideal test ground to start developing these new power electronics improvements, and there are several projects in different locations, but none in the Canary Islands, where most of the electrical power is supplied by combustion machines, despite the major availability of the natural resources.

Nevertheless, regarding the literature, there is still a lack of regulation on GFM systems, so more detailed research and the creation of uniform testing standards are needed to enable quick and secure deployment of GFMs. The Fraunhofer IEE's System Stability and Grid Integration department was engaged in a number of projects in this matter at the time this work was being developed.

Acknowledgements

I want to finish this work by thanking everyone that has made it possible. Starting from my supervisor Gunter Arnold and his colleagues Nils Schäfer and Siddhi Kulkarni, who helped me a lot in understanding the research. I really appreciate the opportunity given by their institution to let me develop this thesis with them.

On the other hand, I want to thank my university supervisor, Benjamín González, who has always advised me wisely.

I also want to thank my Master's colleagues, who have made this 2 years much better than expected. It was a real pleasure meeting them and developing a very good friendship.

And last but not least, I would like to thank everyone that has made my stay in Kassel easier and happier.

References

[1] J. Matevosyan, J. Macdowell, N. Miller, B. Badrzadeh, D. Ramasubramanian, A. Isaacs, R. Quint, E. Quitmann, R. Pfeiffer, H. Urdal, T. Prevost, V. Vittal, D. Woodford, S. H. Huang, and J. O'Sullivan, "A future with inverter-based resources: Finding strength from traditional weakness," *IEEE Power and Energy Magazine*, vol. 19, 2021.

[2] P. Tielens and D. V. Hertem, "The relevance of inertia in power systems," *Renewable and Sustainable Energy Reviews*, vol. 55, pp. 999–1009, 3 2016.

[3] A. Hoke, V. Gevorgian, S. Shah, P. Koralewicz, R. W. Kenyon, and B. Kroposki, "Island power systems with high levels of inverter-based resources: Stability and reliability challenges," *IEEE Electrification Magazine*, vol. 9, 2021.

[4] A. Dyśko, A. Egea, Q. Hong, A. Khan, P. Ernst, R. Singer, and A. Roscoe, "Testing characteristics of grid forming converters part iii : inertial behaviour," *19th Wind Integration Workshop*, 2020.

[5] F. Rauscher, M. Nuschke, and B. Engel, "Determination of the damping and inertia time constant of grid forming inverters by laboratory measurements," in *NEIS 2021 - Conference on Sustainable Energy Supply and Energy Storage Systems*, pp. 1–6, September 2021.

[6] F. Sadeque, D. Sharma, and B. Mirafzal, "Multiple grid-forming inverters in black-start: The challenges," in *2021 IEEE 22nd Workshop on Control and Modelling of Power Electronics (COMPEL)*, pp. 1–6, 2021.

[7] R. H. Lasseter, Z. Chen, and D. Pattabiraman, "Grid-forming inverters: A critical asset for the power grid," *IEEE Journal of Emerging and Selected Topics in Power Electronics*, vol. 8, 2020.

[8] J. Matevosyan and J. MacDowell, "Grid-forming technology in energy systems integration," tech. rep., Energy Systems Integration Group, 2022. https://www.esig.energy/reports-briefs.

[9] C. de Transición Ecológica Lucha contra el Cambio Climático y Planificación Territorial, "Anuario Energético de Canarias 2020," tech. rep., Gobierno de Canarias, Jan. 2022.

[10] "Redata api | red eléctrica." https://www.ree.es/es/apidatos. (Accessed on 06/08/2022).

[11] C. Hachmann, H. Becker, J. Haack, and M. Braun, "Improving the resilience of power system operation - contribution of renewable energies in power system restoration," in *NEIS 2019; Conference on Sustainable Energy Supply and Energy Storage Systems*, pp. 1–6, 2019.

[12] Regatron AG, *TC.GSS Series*, April 2020. https://www.regatron.com/assets/resources/Documents/Technical-Datasheets/TC.GSS/2210_TC.GSS.20.400.4WR.S_datasheet_EN_20200423.pdf.

[13] Ametek, *California Instruments RS Series*, December 2021. https://www.programmablepower.com/products/ac-power-sources/rs-series.

[14] Dewetron, *Technical Reference Guide*, September 2012. https://s3-eu-central-1.amazonaws.com/centaur-wp/theengineer/prod/content/uploads/2014/03/14171000/dewetron_technical-reference-guide_e.pdf.

[15] KoCoS Messtechnik AG, *Specifications EPPE W8*, December 2011. https://www.kocos.com/fileadmin/download/EPPE/Specsheet/ENG/DB_EPPE_W8_122011_ENG.pdf.

[16] "PNE-prEN 50549-10 Requirements for generating plants to be connected in parallel with distribution networks - Part 10: Tests for conformity assessment of generating units." https://tienda-aenor-com.accedys2.bbtk.ull.es/norma-proyecto-pne-pren-50549-10-p0057145, 2022. (Accessed on 30/08/2022).

A RoCoF figures

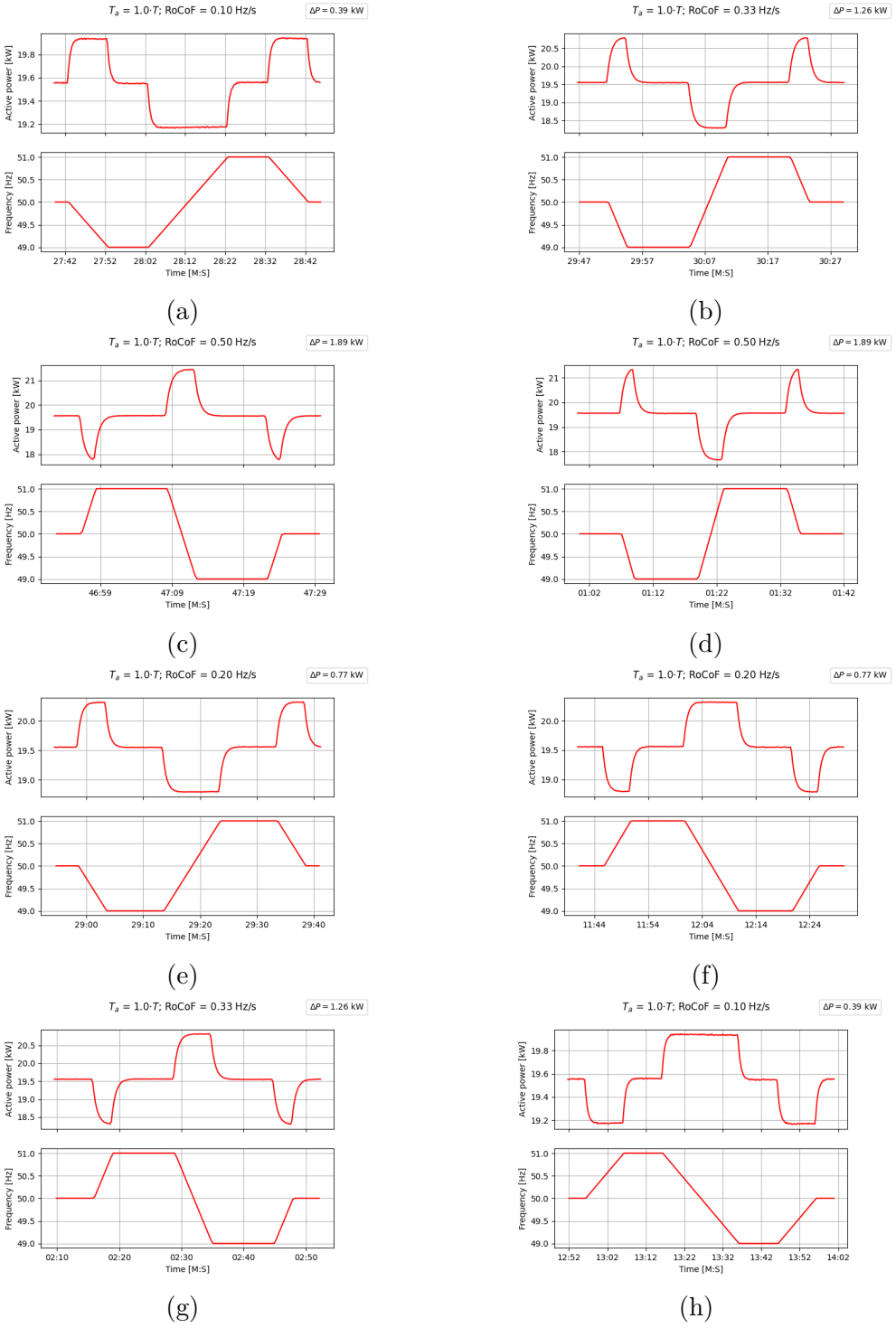

Figure 22: RoCoFs with Ta = 1Ta

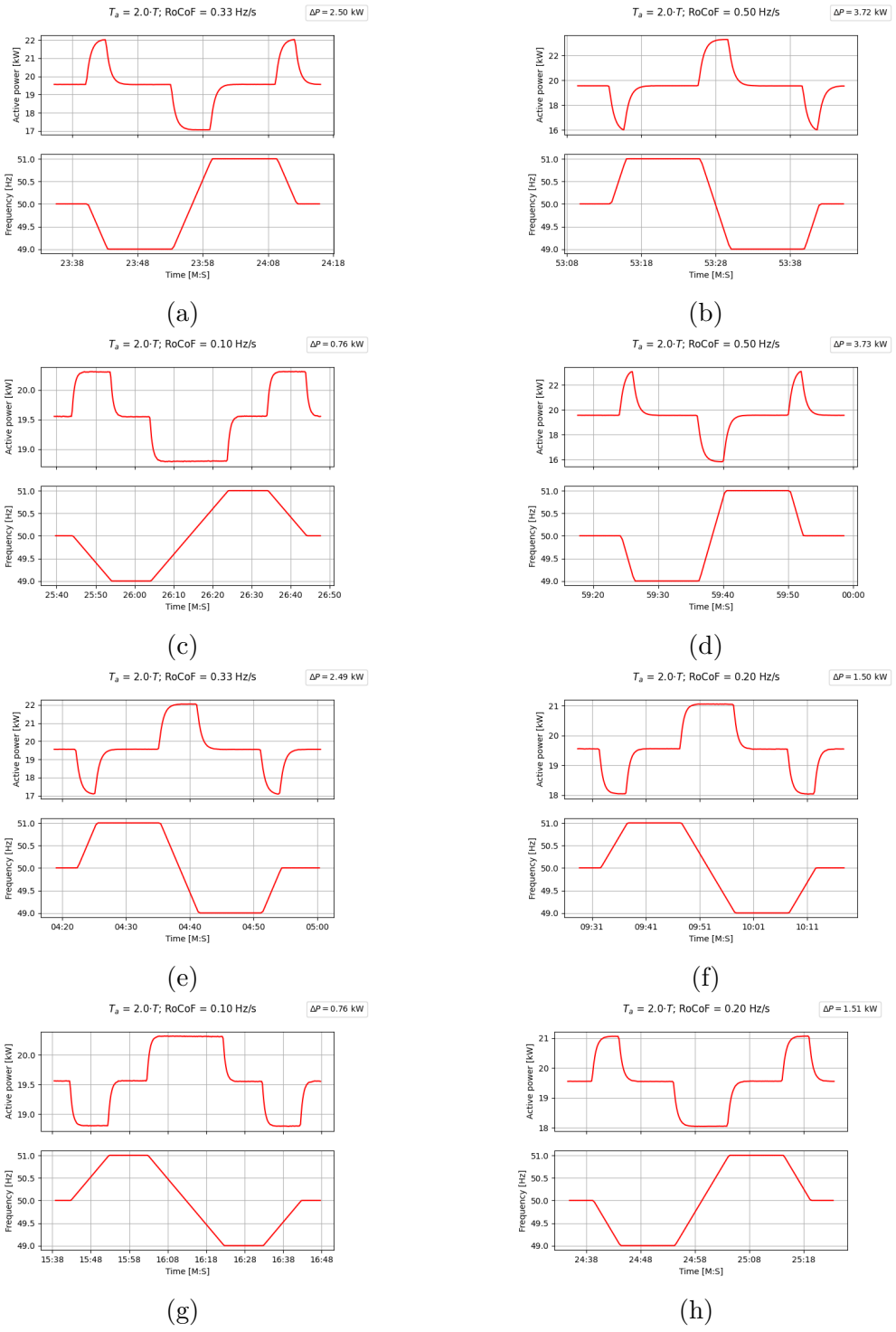

Figure 23: RoCoFs with Ta = 2Ta

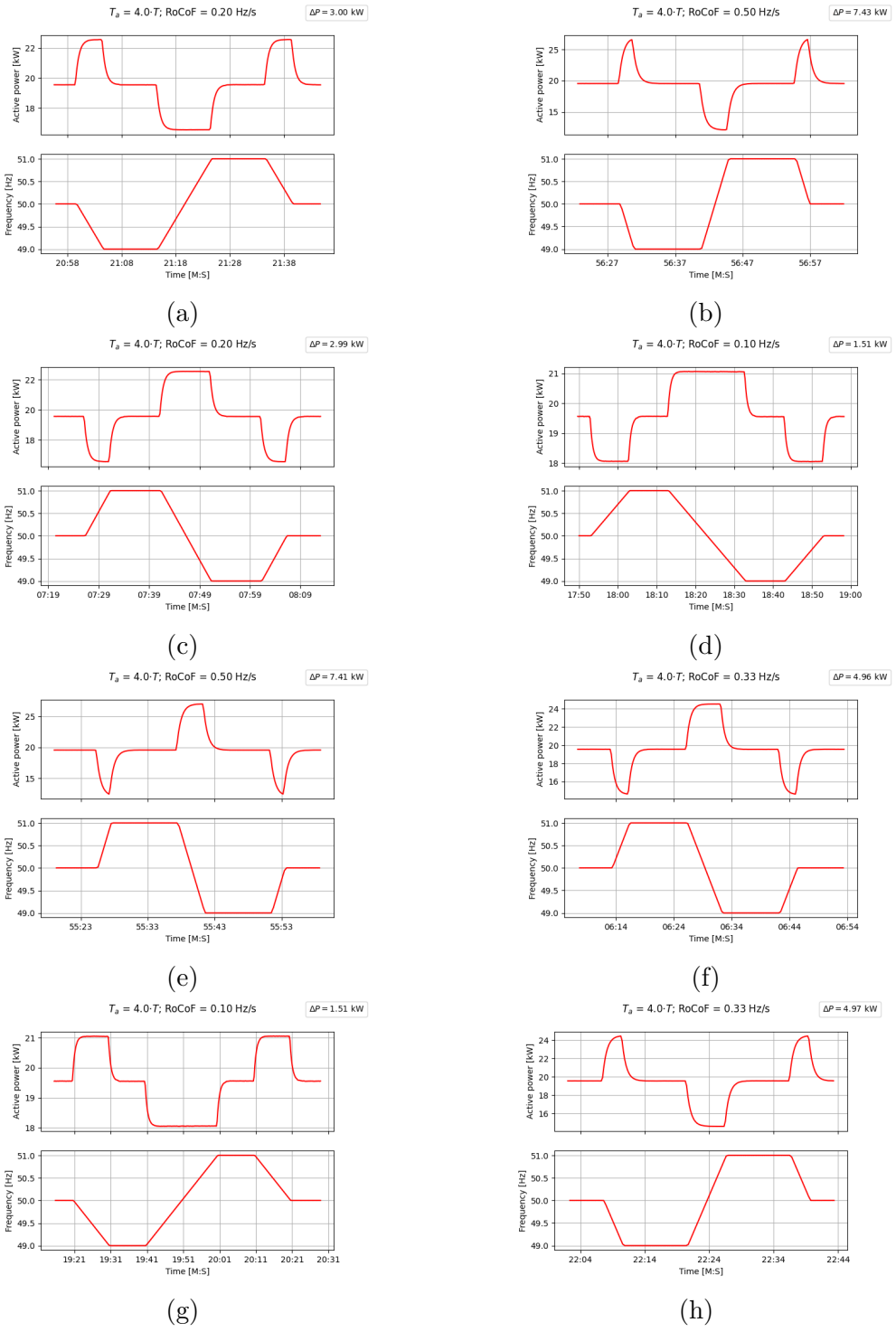

Figure 24: RoCoFs with Ta = 4Ta

B System split figures

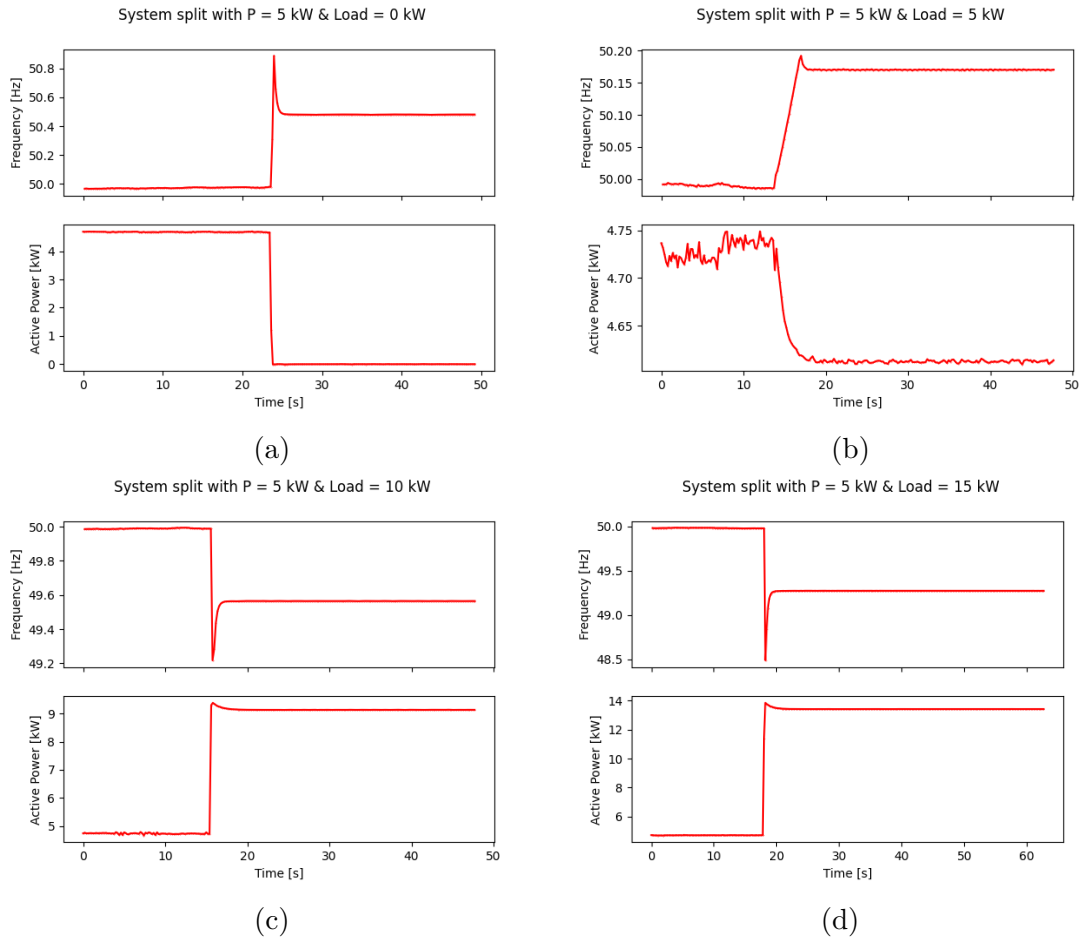

Figure 25: System splits with P = 5kW

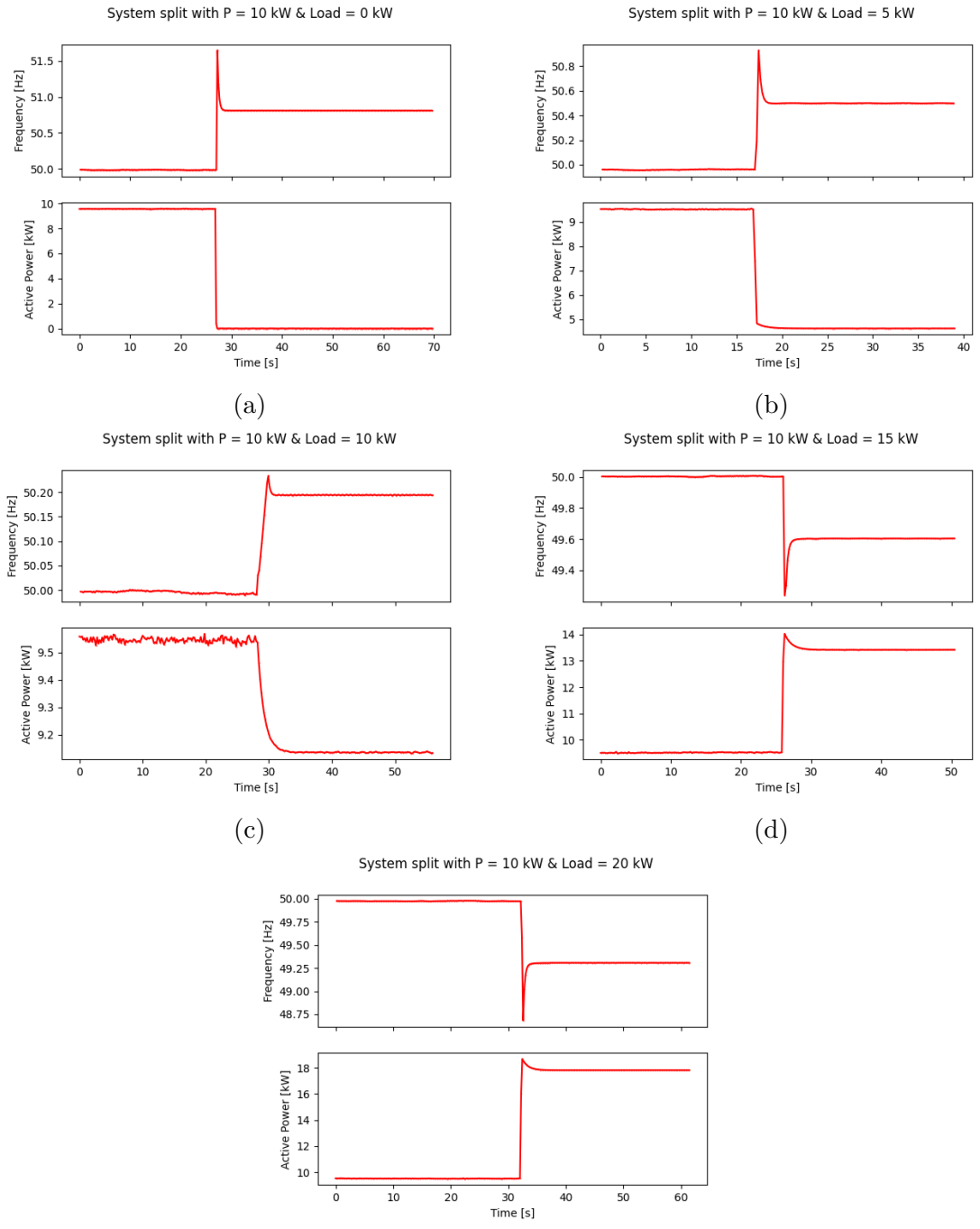

Figure 26: System splits with P = 10kW

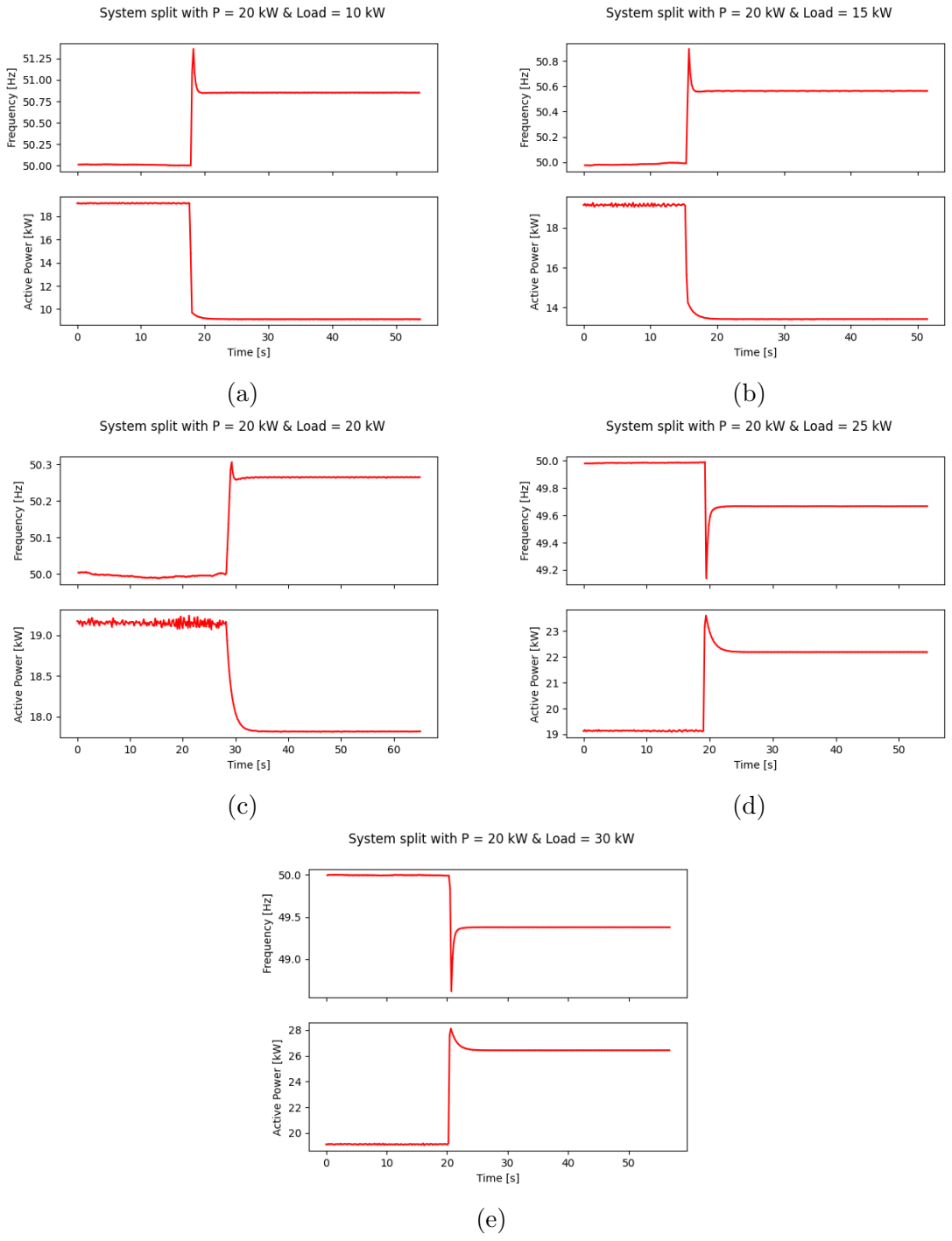

Figure 27: System splits with P = 20kW